

Ultra-High Purity Conditions for Nitride Growth with Low Oxygen Content by Plasma-Enhanced Atomic Layer Deposition

Running Title: UHP Conditions for Nitride Growth by PEALD

Running Authors: Rayner Jr. et al.

G. B. Rayner Jr.,^{1,a)} N. O'Toole,¹ J. Shallenberger² and B. Johs³

¹The Kurt J. Lesker Company, 1925 PA-51, Jefferson Hills, PA 15025

²Materials Research Institute, The Pennsylvania State University, University Park, PA 16802

³Film Sense, 500 W South St #7, Lincoln, NE 68522

^{a)}Electronic mail: brucer@lesker.com

Ultra-high purity (UHP) reactor conditions provide a process environment for growth of nitride thin films with low oxygen content by plasma-enhanced atomic layer deposition (PEALD). In particular, UHP conditions correspond to partial pressures below 10^{-8} Torr for impurities within the PEALD process environment to limit incorporation before, during and after film growth. In this article we identify the various sources of background oxygen species and describe the measures taken to obtain UHP reactor conditions. For example, in situ ellipsometry results are presented that reveal the impact of oxygen incorporation on film resistivity during and after titanium nitride PEALD due to elevated levels of oxygen impurities in the argon process gas. A model is also developed that shows the significance of water permeation through elastomer vacuum seals. These examples demonstrate the importance of process gas purification and elimination of elastomer permeation towards achieving a UHP environment. X-ray photoelectron spectroscopy (XPS) depth profile data for titanium, aluminum and silicon nitride by PEALD reveal bulk oxygen levels below 1 atomic % (at.%), thereby demonstrating the effectiveness of UHP reactor conditions at reducing oxygen incorporation. Consistent with XPS, depth profile secondary ion mass spectroscopy (SIMS) results for titanium nitride PEALD confirm bulk oxygen content less than 1 at.%, further establishing the effectiveness of a UHP background for high purity nitride film growth.

I. INTRODUCTION

Nitride materials by plasma enhanced atomic layer deposition (PEALD) are of significant interest for a wide range of electronic applications including logic, power and optoelectronics devices.¹⁻⁵ One of the challenges for obtaining high-quality nitrides by PEALD is the prevention of oxidation during growth.⁶ This is especially true for nitrides of elements with a high affinity for oxygen such as titanium nitride where reported oxygen levels vary over an extended range.⁷⁻¹¹ Due to the relatively slow deposition rates of nitride materials grown by PEALD, these processes have long suffered from relatively high exposures to background oxygen impurities yielding elevated oxygen levels in the resulting layers. Ultra-high purity (UHP) reactor conditions are based on reduced levels of background oxygen species within the PEALD process environment to limit exposure before, during and after film growth. Creating and maintaining UHP conditions are also important for consistent, reproducible PEALD process results.¹² To define these conditions, it is instructive to consider the specifications for a UHP grade (99.999% purity) process gas, such as argon (Ar), molecular nitrogen (N₂) and molecular hydrogen (H₂), and the associated exposure to oxygen species during growth. A similar approach was recently reported in the literature.⁶

UHP grade Ar contains oxygen impurities up to the part-per-million (ppm) level. These impurities include molecular oxygen (O₂), water (H₂O), carbon monoxide (CO) and carbon dioxide (CO₂). For Ar at 1 Torr chamber pressure, the ppm level corresponds to 10⁻⁶ Torr partial pressure. For an impurity such as H₂O at 10⁻⁶ Torr partial pressure, a growing nitride surface experiences 1 Langmuir H₂O exposure every second (sec) where 1 Langmuir = 10⁻⁶ Torr·second. Under these conditions, if each H₂O molecule striking the surface adsorbs (or sticks), then ~1 monolayer surface coverage would be subsequently obtained each second. A typical PEALD process deposits less than a monolayer of material per each complete cycle (one complete cycle =

one full sequence of precursor dose and purge steps). Typical PEALD cycle times range from 10-60 seconds. Therefore, each sub-monolayer of material deposited experiences 10-60 Langmuir exposures (or 10-60 “monolayer-equivalent” exposures) from each impurity present in the reactor at the ppm level every second. These conditions will result in elevated levels of oxygen in the deposited nitride film. By decreasing oxygen impurities below 0.01 ppm, or 10 part-per-billion (ppb), the corresponding partial pressures (at 1 Torr Ar pressure) are below 10^{-8} Torr. For oxygen impurities below 10^{-8} Torr partial pressure, 1 Langmuir exposure requires >100 seconds such that exposure to impurities such as H₂O are significantly reduced during typical PEALD cycle times. UHP conditions are defined here as partial pressures < 10^{-8} Torr for background oxygen impurities within the PEALD process environment. In this article we identify the various sources of background oxygen species and describe the measures taken to obtain UHP reactor conditions. To investigate the effectiveness of UHP reactor conditions at reducing oxygen contamination, various nitrides were grown by PEALD in a UHP process environment. These nitrides were subsequently characterized to determine the oxygen content in the bulk of the films.

II. EXPERIMENTAL

A. Film Deposition

Depositions were performed in a Kurt J. Lesker Company ALD150LX perpendicular-flow reactor equipped with a chemical series vacuum pump [nominal pumping speed = 44 cubic feet per minute (cfm) = 21 Liters/sec (L/s)]. Plasma was generated by a remote inductively coupled plasma (ICP) source operating at 13.56 Megahertz (MHz) frequency and 975 Watt (W) plasma power. A fused silica (SiO₂) plasma tube provided a transparent window for radio frequency (RF) signal transmission between an external, silver-coated copper, RF coil and the plasma gas.

Analytical ports (70° angle of incidence) equipped with fused silica viewports enabled in situ process monitoring by ellipsometry. An integrated load-lock equipped with a turbomolecular pump [nominal pumping speed (N₂) = 52 L/s] was used for sample transfer. The load-lock pressure prior to sample transfer was < 2x10⁻⁵ Torr. A rectangular gate valve provided isolation between the load-lock chamber and the PEALD reactor.

Titanium nitride (TiN_x), aluminum nitride (AlN_x) and silicon nitride (SiN_x) PEALD were performed at ~1 Torr pressure on untreated 150 mm silicon (100) wafers (with a native or 1000 nm thermal oxide surface layer). The process gases used were Ar, N₂ and H₂ (99.999%, Praxair). For TiN_x growth, two different titanium (Ti) precursors were used: titanium tetrachloride (TiCl₄) and tetrakis-dimethylamino titanium (TDMAT). The TiCl₄ and TDMAT precursors (Strem Chemicals, Inc.) were maintained at room temperature and 82°C, respectively. TiN_x PEALD was performed at 350°C substrate temperature using TiCl₄ and a mixture of Ar, H₂ and N₂ (Ar-H₂-N₂) plasma species (TiN#1). Plasma gas flow rates were 160 sccm Ar, 15 sccm H₂ and 5 sccm N₂. A complete PEALD cycle consisted of the following steps: (1) 0.1 sec TiCl₄ dose, (2) 3 sec purge, (3) 8 sec Ar-H₂-N₂ plasma dose, (4) 5 sec purge (cycle time = 16.1 seconds). The growth-per-cycle (GPC) was 0.33 Å/cycle. The TDMAT process (TiN#2) utilized an Ar-N₂ plasma mixture at 250°C substrate temperature (GPC = 0.75 Å/cycle). The Ar and N₂ flow rates through the ICP were 160 and 25 sccm, respectively. A complete PEALD cycle consisted of (1) 0.7 sec TDMAT dose, (2) 3 sec purge, (3) 22 sec Ar-N₂ plasma dose, (4) 5 sec purge (cycle time = 30.7 seconds). The aluminum (Al) and silicon (Si) precursors used were trimethylaluminum (TMA) and tris-dimethylamino silane (3DMAS), respectively (Strem Chemicals, Inc.). Both precursors were kept at room temperature. AlN_x and SiN_x PEALD utilized Ar-N₂ plasma (160 sccm Ar and 50 sccm N₂) at substrate temperatures of 300°C and 350°C, respectively. Static dosing was utilized for

TMA and 3DMAS precursors (i.e., consisted of dose and exposure steps with no active pumping). A complete PEALD cycle consisted of (1) 0.26/0.5 sec TMA/3DMAS dose, (2) 4 sec exposure, (3) 5 sec purge, (4) 12 sec Ar-N₂ plasma dose, (5) 5 sec purge (cycle time \cong 26 seconds). The GPC was 1.5 Å/cycle for the AlN_x process, and 0.13 Å/cycle for SiN_x PEALD.

B. Film Characterization

Film thickness and optical properties were determined ex situ by spectroscopic ellipsometry (SE) using a J. A. Woollam M-2000 spectroscopic ellipsometer over a range of wavelengths from 193-1000 nm. For TiN_x, a Drude-Lorentz model was used to analyze the SE data and extract film thickness and optical resistivity.^{13,14} A Cauchy model was used to determine the thickness and index of the AlN_x and SiN_x layers. Ellipsometry measurements were also performed in situ to determine film thickness and resistivity during TiN_x growth (TiCl₄ process) using a Film Sense FS-1EX multi-wavelength ellipsometer. The FS-1EX ellipsometer provides 6 wavelengths of ellipsometric data (405, 450, 525, 660, 850 and 950 nm). For the in situ measurements, TiN_x films were deposited on 1000 nm thermal oxide on 150 mm Si (100) substrates. TiN_x resistivity was further investigated ex situ by SE and four point probe techniques. Four point probe (4pp) measurements utilized a Jandel MWP-6 multiposition wafer probe equipped with a Keithley 2410 SourceMeter to determine TiN_x sheet resistance. The TiN_x sheet resistance was multiplied by the corresponding SE film thickness to obtain electrical resistivity.

Film composition was measured by depth profile x-ray photoelectron spectroscopy (XPS) using a Physical Electronics VersaProbe II instrument equipped with a monochromatic Al K α x-ray source [1486.7 electron volts (eV)] and a concentric hemispherical analyzer. To optimize the analysis for carbon and oxygen (two elements common to the background levels in XPS), the

samples were pre-pumped overnight in the analytical chamber while cycling a titanium sublimation pump. This resulted in background levels of carbon (C) and oxygen (O) at $\sim 0.5 \pm 0.2$ atomic % (at.%). Quantification utilized instrumental relative sensitivity factors (RSFs) that account for the x-ray cross section and inelastic mean free path of the electrons. For the major elements (Ti, Al, Si, N), the 1 sigma (1σ) quantitative accuracy is expected to be within ± 10 relative % (rel%). Due to poor counting statistics, and finite backgrounds of C and O, the 1σ accuracy is expected to be within ± 20 -40 rel% for the minor elements. Ion sputtering was accomplished using a 2 kilovolt (kV) Ar^+ ion beam. Elemental depth profiling was also performed by secondary ion mass spectroscopy (SIMS) utilizing a Physical Electronics (PHI) Adept 1010 quadrupole instrument. Measurements utilized 1 kV cesium⁺ (Cs^+) ion bombardment. Negative ions were detected. Elemental quantification was based on RSFs calculated from an implanted TiN film reference material. The 1σ quantitative accuracy is expected to be ± 5 -30 rel%.

III. RESULTS AND DISCUSSION

A. Background Oxygen

Background oxygen impurities inside a typical PEALD reactor originate from the following six sources: (1) system leaks, (2) process gases, (3) elastomer permeation, (4) process pump back-diffusion, (5) outgassing and (6) plasma etching. All system components were thoroughly leak tested to ensure no atmospheric leaks, and no internal leaks of process gas and/or vapor across valve seats. Process gases are a primary source of background oxygen species. Therefore, gas purifiers (SAES Micro Torr / Entegris Gatekeeper) were installed on the primary delivery lines for Ar, N_2 and H_2 which reduce oxygen impurities below the ppb level. As discussed previously, UHP grade process gases contain up to ppm levels of oxygen impurities such as O_2 and H_2O . In addition,

improper maintenance of the source gas, delivery lines and/or components (e.g., routine gas cylinder changeover) can result in impurity concentrations exceeding the ppm level. These variations result in a wide range of oxygen contamination levels in nitride layers by PEALD which can have a significant impact on nitride film properties such as resistivity. For example, the data presented in Fig. 1 show TiN_x resistivity vs. time (during TiN_x PEALD using TiCl_4 and $\text{Ar-H}_2\text{-N}_2$ plasma at 350°C) with and without Ar gas purification. The films were deposited on 1000 nm thermal oxide on Si. Baseline conditions in Fig. 1 correspond to active purification of the Ar process gas.

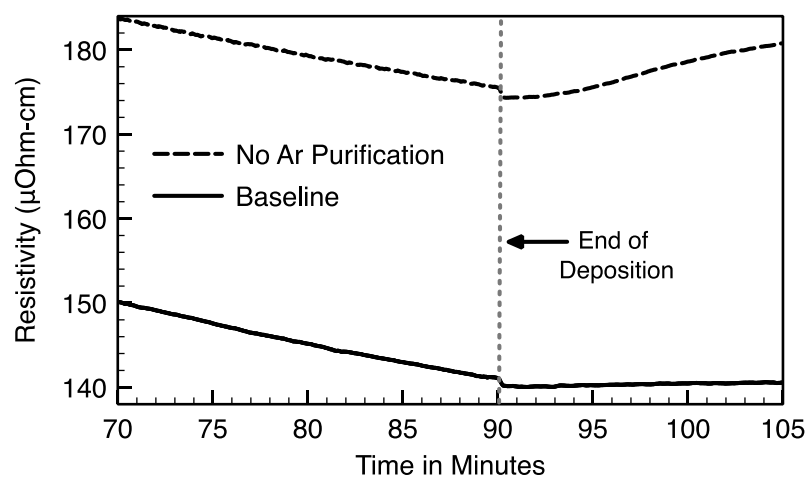


FIG. 1. TiN_x resistivity vs. time monitored in situ by multi-wavelength ellipsometry demonstrating the effect of oxygen incorporation during and after film growth with no Ar purification.

The TiN_x films were measured in real-time during and after the deposition by in situ multi-wavelength ellipsometry (MWE). The data were acquired at 1 second time intervals and analyzed by a Drude-Lorentz model to determine the film thickness and resistivity vs. time.^{13,14} The final thickness was ~ 11 nm for both TiN_x films (not shown). There are several important features to note in Fig. 1. First, the film resistivity decreases during the deposition due to increasing grain

size and reduced surface scattering. Second, the resistivity is significantly higher with no Ar purification (compared to the baseline process which uses Ar purification) due to higher oxygen content in the film. Lastly, without Ar purification the film resistivity increases after the deposition, while the baseline process is stable. The changes in the in situ ellipsometry data after the deposition of the sample with no Ar purification are *not* consistent with the growth of a surface oxide (e.g., TiO₂), but are best modeled by a change in the film dielectric function corresponding to an increase in resistivity. This observation is consistent with previous results,¹⁵ and the increase in TiN_x resistivity after the deposition is likely due to diffusion of residual oxygen from the process gas into the film through grain boundaries, resulting in a mixed TiO_yN_x phase. From in situ ellipsometry measurements alone it is not possible to determine the depth profile of the residual oxygen in the film, but it is probable that the near surface would have a higher oxygen content.

TABLE I. Summary of in situ MWE, and ex situ SE & 4pp results for TiN_x PEALD. The error bars on the ellipsometrically determined values are the 90% confidence limits from the fit statistics.

<i>Conditions - TiCl₄ Process</i>	<i>MWE Thick. (nm)</i>	<i>SE Thick. (nm)</i>	<i>MWE Res. (μOhm-cm)</i>	<i>SE Res. (μOhm-cm)</i>	<i>4pp Res. (μOhm-cm)</i>
Baseline	10.5 ± 0.17	10.7 ± 0.048	141 ± 2.9	124 ± 1.2	151 ± 10
Baseline	34.0 ± 0.64	34.5 ± 0.11	99 ± 3.6	87 ± 0.8	86 ± 10
No Ar Pur.	11.1 ± 0.22	11.2 ± 0.053	184 ± 4.5	168 ± 1.7	243 ± 10
No Ar Pur.	37.2 ± 0.96	37.7 ± 0.11	140 ± 6.5	130 ± 1.0	154 ± 10

TiN_x resistivity was further investigated ex situ by SE and 4pp techniques. These results are summarized in Table I. TiN_x films were also deposited with increased thickness to minimize the effects of surface scattering on film resistivity. The MWE resistivities in Table I represent the

final values determined just prior to removal from the PEALD reactor. In contrast to SE measurements at room temperature, MWE measurements were performed at 350°C resulting in slightly higher values for MWE resistivity. TiN_x resistivity increases with temperature due to an increase in electron-phonon scattering, which results in a decrease in the electron mean free path.¹⁴ The 4pp measurements were also performed at room temperature. For the 34 nm baseline film, 4pp resistivity is essentially identical to SE resistivity, but the 11 nm baseline film is 27 μOhm-cm higher. These results suggest that 4pp resistivity has greater sensitivity to post-oxidation of the TiN_x surface.

Without Ar purification, the 4pp resistivity is 75 μOhm-cm higher than the SE value for the 11 nm film; however, this difference is reduced to 24 μOhm-cm for the 37 nm film thereby demonstrating a strong thickness dependence. As discussed above, the increase in TiN_x resistivity observed after the deposition in Fig. 1 is likely due to diffusion of residual oxygen from the process gas into the bulk of the film through grain boundaries. The near surface region is expected to contain a higher oxygen concentration which could account for differences between 4pp and SE resistivity, including the strong thickness dependence, observed in Table I for film growth without Ar gas purification. These results emphasize the importance of process gas purification for creating and maintaining UHP conditions.

Elastomer permeation is another source of background oxygen impurities that warrants careful consideration. Elastomers are commonly used to create vacuum seals between system components. Permeation is the transport of gases through a solid barrier/material by diffusion. Although it applies generally to all materials, the rates are typically low enough that it can be ignored. However, gases and/or vapors can readily diffuse through elastomers such that permeation does become an important factor for creating and maintaining UHP conditions.

Elastomers contain small openings (or voids) that readily enable diffusion of gases/vapors through the bulk of the material. These materials consist of large, interwoven molecular chains resulting in a microstructure that is more open as compared to materials such as ceramics and metals. The permeation rate, given in units of $\text{cm}^3(\text{STP})/\text{sec}$, is represented by the equation: $Q = K(A/L)\Delta P$, where K is the temperature-dependent permeation coefficient, A is the surface area through which gas/vapor phase species enter the elastomer, L is the thickness of the material (i.e., the permeation length), and ΔP is the partial pressure difference across the elastomer for a given species.¹⁶⁻¹⁸ Note that STP implies standard temperature ($0^\circ\text{C} = 273.15$ Kelvin) and pressure ($1 \text{ atm} = 760 \text{ Torr}$).

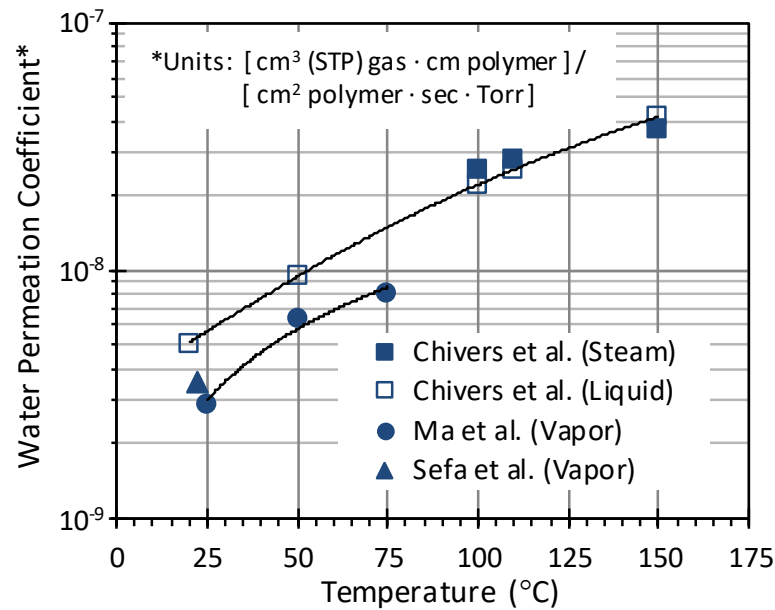


FIG. 2. Permeation coefficient (or permeability) vs. temperature for water (in the liquid, steam and vapor phase) through Viton over a range of temperatures.

This equation assumes steady-state diffusion and that adsorbed molecules do not dissociate. The steady-state permeation rate can also be expressed to explicitly show temperature dependence: $Q = K_0 e^{-E/RT} (A/L)\Delta P$, where the pre-exponential factor K_0 is a constant, E is the activation energy of

diffusion, R is the gas constant and T is temperature (K_0 and E are gas and material dependent). In general, the permeation coefficient K increases with temperature. Fig. 2 shows the water permeation coefficient (or permeability) for Viton vs. temperature.

The data points in Fig. 2 are from Chivers (water – liquid & steam), Ma (water vapor) and Sefa (water vapor) where the lines serve to guide the eye.¹⁹⁻²¹ It is notable that permeability increases by $\sim 10x$ between room temperature and 150°C , thereby demonstrating a strong temperature dependence. Water is of primary interest here because of its relatively high permeation rate through elastomer materials, as well as its associated impact on background oxygen levels in a PEALD process environment. Sefa et al. used the circular o-ring configuration illustrated in Fig. 3 to approximate the permeation rate of H_2O through Viton.²¹ In Fig. 3, the o-ring is compressed between two planar sealing surfaces forming an elliptical or oval shape. The approximate surface area A exposed to H_2O at partial pressure P_1 is as follows: $A = \pi Dh$, where D is o-ring diameter and h is the compressed height. Inserting this into the permeation rate relationship gives the following equation: $Q \cong K(\pi Dh/L)\Delta P$, where the permeation length L is approximately the compressed width of the o-ring and $\Delta P (= P_1 - P_2)$ is the partial pressure difference of water vapor across the seal as illustrated in Fig. 3. For example, let P_1 equal the partial pressure of water in atmosphere at 2.0% atmospheric pressure (22°C , 75% relative humidity), and let P_2 be the H_2O partial pressure in an ALD process environment. In this case $P_1 \gg P_2$ such that $\Delta P \cong 15$ Torr. Using the results from Fig. 2, $K \cong 3.7 \times 10^{-8}$ [$\text{cm}^3(\text{STP}) \text{ gas} \cdot \text{cm polymer} / [\text{cm}^2 \text{ polymer} \cdot \text{sec} \cdot \text{Torr}]$] for Viton at 150°C . For a single Viton o-ring with $D = 13.6$ cm (= 5.35 inches), $d = 0.50$ cm (0.20 inches), $h = 0.40$ cm (0.16 inches) and $L = 0.53$ cm (0.21 inches), the H_2O permeation rate $Q = 1.8 \times 10^{-5} \text{ cm}^3(\text{STP})/\text{sec} = 2.1 \times 10^{-5} \text{ Torr} \cdot \text{L}/\text{s}$. Based on pumping speed = 21 L/s, the background partial pressure of water is $\sim 10^{-6}$ Torr, or ~ 1 Langmuir

exposure every second. To meet UHP conditions, only metal and differentially pumped elastomer seals were used (including o-ring seals around the fused silica ICP tube), with the exception of o-rings positioned downstream relative to the substrate location. Differentially pumped seals consist of two o-rings and a port for creating vacuum between the seals.

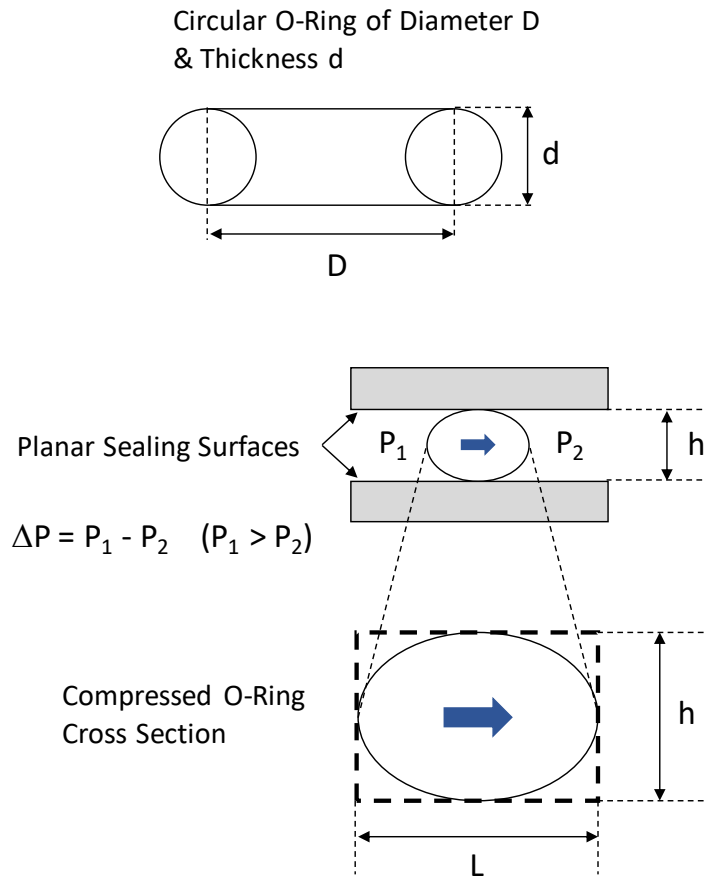


FIG. 3. Elastomer o-ring configuration used to approximate water permeation rate through Viton.

A schematic of the ICP source used for this work is presented in Fig. 4(a) which illustrates the differentially pumped seal configuration around the top (inlet) and bottom (outlet) of the fused silica ICP tube. The two flange-adapter assemblies in Fig. 4(a) are removed from the ICP tube to better illustrate the various components. In Fig. 4(b), the outlet flange-adapter is shown fully

assembled. The inlet flange-adapter is assembled in a similar fashion (not shown). A port is provided to draw vacuum within the volume between each pair of Viton o-rings located at the inlet and outlet tube connections. By reducing the pressure below ~ 0.1 Torr within each volume, permeation through the elastomer seal connections can be substantially reduced. Water cooling (not shown) of the outlet flange-adapter was also employed to prevent overheating of the Viton o-rings during operation at 975 W plasma power.

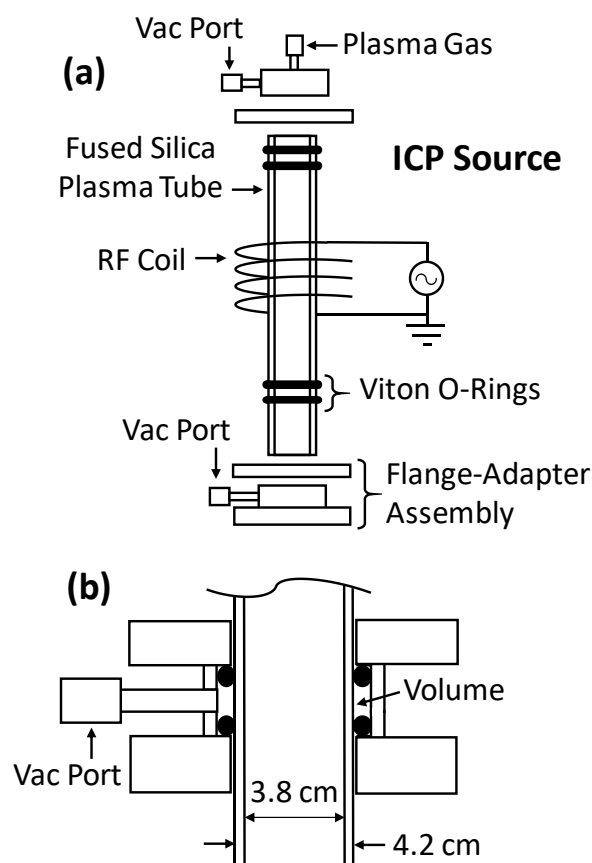


FIG. 4. (a) Schematic of the ICP source used for this work illustrating the differentially pumped seal configuration at the top (inlet) and bottom (outlet) of the fused silica ICP tube. The inlet/outlet flange adapter assemblies are removed from the ICP tube to better illustrate the various components. (b) The outlet adapter flange is shown fully assembled.

A schematic of the PEALD reactor is presented in Fig. 5, illustrating the various vacuum seal connection points. All process gas line connections utilized metal seals, including the plasma gas (A) and precursor vapor (B) connections in Fig. 5. The connection between the ICP and chamber lid (C), as well as connections between the fused silica viewports and chamber analytical ports (E), also include metal seals. The connection between the lid and chamber (D) incorporated a differentially pumped elastomer seal.

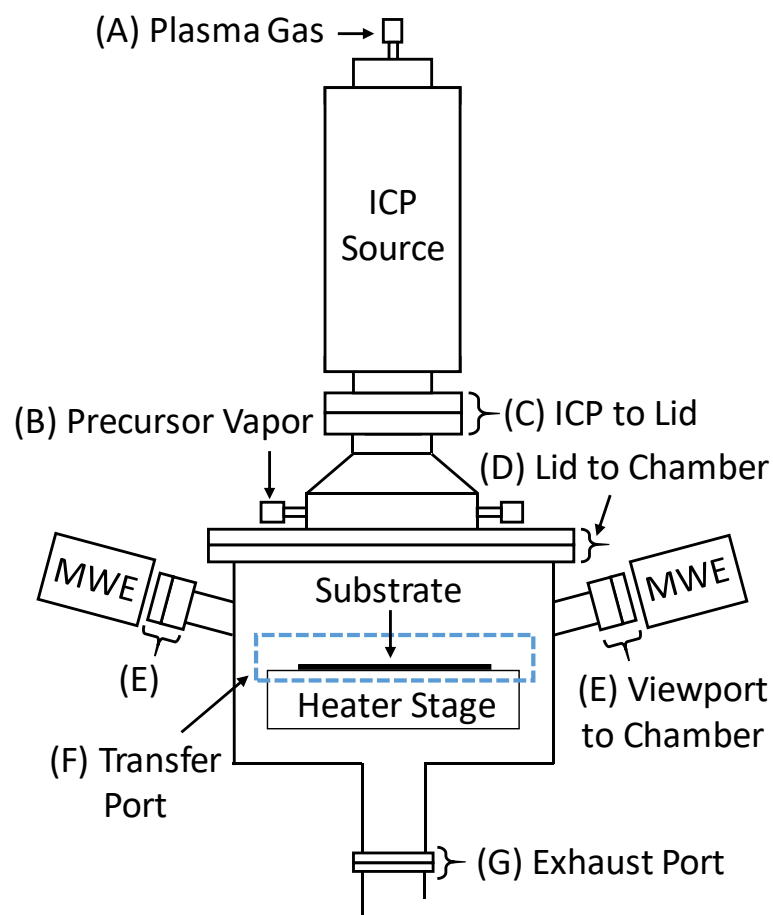


FIG. 5. A schematic representation of the PEALD reactor used for this work illustrating the various vacuum seal connection points.

For clarity, only an outline of the substrate transfer port (F) is included in Fig. 5. As previously described, a rectangular gate valve was used to provide isolation between the reactor and load lock chamber. The gate valve was opened during wafer transfer in/out of the reactor; otherwise, it remained closed. The connection point between the transfer port flange and gate valve (not shown) was also a differentially pumped elastomer seal. Elastomer seals located downstream, e.g., exhaust port (G), did not require differential pumping since viscous-laminar flow through the reactor was maintained, thereby preventing back-diffusion of impurities due to downstream permeation. The reactor process pressure and gas flow conditions are discussed in more detail below.

The inner and outer diameters of the ICP tube in Fig. 4 are 3.8 cm (1.5 inches) and 4.2 cm (1.7 inches), respectively. In this differentially pumped configuration, four Viton o-rings are used, each having the following dimensions: $D = 4.6$ cm (= 1.8 inches) and $d = 0.50$ cm (= 0.20 inches). In a more common configuration, without differential pumping, only two o-rings would be utilized (i.e., one o-ring at the inlet, and one o-ring at the outlet of the ICP tube). In this non-differentially pumped configuration, a portion of each o-ring's surface area would be exposed to atmosphere, resulting in adsorption and subsequent diffusion (i.e., permeation) of atmospheric components through the o-ring, and into the internal volume of the reactor. Using the approach for H₂O permeation through Viton described above, the permeation rate Q at 150°C is 1.4×10^{-5} Torr·L/s. At room temperature, $Q = 1.4 \times 10^{-6}$ Torr·L/s which is a 10x reduction in throughput. Since the o-ring temperature is typically between these two limits, the average permeation rate provides a reasonable approximation for estimating background oxygen due to permeation. Using the average value of 7.7×10^{-6} Torr·L/s (pumping speed = 21 L/s), the background partial pressure of water is $\sim 4 \times 10^{-7}$ Torr, or ~ 1 Langmuir exposure every 2.5 seconds. At this background level,

oxygen concentrations >1 at.% are likely for nitride materials that have a strong tendency to oxidize during growth. These calculations demonstrate that o-ring seals around the inlet and outlet of the ICP tube should be differentially pumped to achieve UHP conditions.

In general, background impurity levels may be substantially reduced by lowering the base pressure of the reactor. A relevant example of this is epitaxial Si growth by conventional chemical vapor deposition (CVD) techniques. Similar to many nitrides, single crystal elemental Si has a strong tendency to oxidize during growth. For Si epitaxy at low temperature and pressure, Meyerson established that a base pressure below 10^{-8} Torr provided a suitable process environment for high quality Si growth.^{22,23} Mechanical pumps provide a minimum base pressure of $\sim 10^{-2}$ to 10^{-4} Torr. To achieve base pressures below 10^{-4} Torr, PEALD reactors routinely utilize turbomolecular pumps.⁸⁻¹¹ In addition to lower base pressure, turbomolecular pumps allow plasma processing at reduced pressures typically ranging from a few to several hundred mTorr.

For remote ICP reactors operating in this low pressure regime, ion energy at the surface of a grounded substrate is typically below 50 eV.²⁴ Substrate biasing can also be used to control the energy of ions impacting the surface during PEALD over a wide range, which enables tuning of material properties as well as reduced oxygen content in nitride films.²⁴⁻²⁶ At lower process pressure and gas flow, however, unwanted precursor exposure and subsequent film deposition on critical/sensitive surface inside the reactor may occur. Unwanted deposition occurs as a result of an insufficient gas diffusion barrier to protect these surfaces during precursor dose and purge steps. For example, deposition of a thin, highly conductive TiN_x layer on the internal ICP tube surface shown in Fig. 4 could cause signal attenuation followed by loss of plasma. To avoid deposition on the internal surface of the ICP tube, an isolation valve can be utilized, but the mechanical actuation

of valving between the ICP source and substrate can generate particles that result in unwanted film defects.

Gas diffusion barrier performance is highly dependent on geometry, pressure and gas flow rate. To create an effective diffusion barrier, gas flow must be viscous and laminar. A general requirement for viscous flow is that characteristic reactor dimensions (e.g., cylindrical tube diameter) should exceed $\sim 100\times$ the mean free path of the background process gas.^{16,17,27} The mean free path λ is represented by the equation $\lambda = kT/(2^{1/2}\pi\sigma^2P)$, where k is the Boltzmann constant (1.381×10^{-23} J/K), T is the temperature (K), σ is the molecular diameter (m) and P is the pressure (Pa). For Ar ($\sigma = 3.64 \times 10^{-10}$ m) at 1 Torr (133.3 Pa) pressure (gas temperature = $150^\circ\text{C} = 423.15$ K), the mean free path λ is $\sim 7\times 10^{-5}$ m = 0.007 cm (0.003 inches). In this case, characteristic dimensions of the reactor should be > 0.7 cm (0.3 inches) to ensure viscous flow conditions. If the pressure is reduced to 0.1 Torr, then critical reactor dimensions should exceed 7 cm (3 inches). For cylindrical (or tubular) reactor geometries at 0.1 Torr pressure, the diameter should exceed 7 cm (3 inches) to ensure viscous flow.

Typical remote ICP reactors, therefore, require process pressures exceeding a few hundred mTorr to achieve viscous flow conditions through the reactor, including associated ports/features (e.g., ports/features for substrate transfer, in-situ ellipsometry and inductive plasma). For process pressures above ~ 100 mTorr (0.1 Torr), turbomolecular pumping speeds markedly decrease to levels at or below typical mechanical pumps with speeds ranging from approximately 5 to 50 L/s. During PEALD processing at pressures > 100 mTorr, this reduction in turbomolecular pumping speed marginalizes the benefit of lower base pressure on background impurities, such as H_2O impurities due to elastomer permeation. To maintain a higher pumping speed, and lower pressure at the pump inlet, a pressure control valve (positioned upstream between the reactor and

turbomolecular pump) is often used in conjunction with reduced gas flow. In this configuration, the reactor pressure can be independently controlled at levels above the pump inlet pressure, including pressures exceeding a few hundred mTorr to ensure viscous flow. The corresponding effective pumping speeds, in this case, remain consistent with the typical range of mechanical pump speeds indicated above. For example, given reactor pressure $P = 0.4$ Torr, temperature $T = 150^\circ\text{C}$ and flow rate Q ranging from 100 to 1000 sccm (or 2 to 20 Torr·L/s), the effective pumping speed S_{eff} ($S_{\text{eff}} = Q/P$) ranges from 5 to 50 L/s, respectively. In addition to gas flow that is viscous, the flow rate must be high enough to prevent back-diffusion of unwanted species (e.g., back-diffusion of unwanted species into the ICP tube where plasma is generated). At pressures required for viscous flow, as well as gas flow rates necessary to create an effective diffusion barrier, mechanical pumps enable high throughput with minimal variation in pumping speed. In this case, however, plasma operation is generally limited to a few hundred mTorr.

Viscous flow is laminar (vs. turbulent) when the Reynold's number is below 1100 (i.e., $Re < 1100$).¹⁷ Based on typical PEALD process conditions (i.e., temperatures, gas flow rates, pressures), $Re \ll 1100$ for cylindrical geometries, thereby satisfying the condition for viscous-laminar flow. For this work, viscous-laminar Ar flow was maintained at ~ 1 Torr pressure. The total Ar flow was ~ 1000 sccm, which served not only as a carrier/purge gas during precursor dose/purge steps, but also as an effective diffusion barrier to prevent back-diffusion of precursor vapor into the ICP tube, analytical ports and transfer port.²⁸ Moreover, continuous viscous-laminar flow inhibits back-diffusion of downstream impurities (i.e., below the substrate in Fig. 5), including oxygen species due to o-ring permeation, as well as other impurities from the reactor foreline and/or vacuum pump.

Finally, to ensure sufficient outgassing of any adsorbed water on internal components, the majority of the reactor surfaces were continuously heated and purged with UHP Ar process gas. In particular, delivery source components directly exposed to precursor vapor were kept at 150°C to prevent long residence times within delivery channels. The reactor lid assembly and walls were maintained at 160°C and 165°C, respectively. Al cladding surrounded by heater jackets were used on all delivery components (including the reactor lid) to achieve temperature uniformity. Outgassing of adsorbed H₂O on non-heated reactor surfaces (e.g., non-heated sections of process gas delivery lines and components) was achieved by purging these components with UHP Ar prior to UHP processing.

B. Film Composition

To obtain UHP reactor conditions, each source of background oxygen described above was systematically addressed, including system leaks, process gases, elastomer permeation, process pump back-diffusion and outgassing. For compositional analysis, TiN_x, AlN_x and SiN_x films were deposited on native oxide on 150 mm Si. The SE thicknesses for TiN#1 (TiCl₄ process), TiN#2 (TDMAT process), AlN_x and SiN_x films were 33, 39, 30 and 18 nm, respectively. In all cases, the thickness non-uniformity was < 3% (1 σ). The optical resistivities for TiN#1 and TiN#2 were 90 and 182 $\mu\text{Ohm-cm}$, respectively (1 σ non-uniformity < 5%). From the SE data (at 633 nm wavelength), the index of refraction was 2.01 for AlN_x and 1.98 for SiN_x. In both cases, the 1 σ index non-uniformity was < 1%.

XPS depth profiles for TiN#1 (TiCl₄ process) and TiN#2 (TDMAT process) are shown in Fig. 6(a) and Fig. 6(b), respectively. These results demonstrate an average oxygen concentration below 1 at.% in the bulk of each film. The oxygen concentrations for TiN#1 and TiN#2 were averaged between 1.6-4.6 and 1.2-5.2 minute (min) sputter time, respectively, to obtain the bulk values. These bulk averages correspond to 0.7 at.% O for TiN#1 in Fig. 6(a), and 0.6 at.% O for TiN#2 in Fig. 6(b). Since these oxygen levels were close to the expected XPS background, depth profile secondary ion mass spectroscopy (SIMS) measurements were also performed. The corresponding SIMS profiles are presented in Fig. 7. In this case, the oxygen concentrations (in atoms/cm³) for TiN#1 and TiN#2 were averaged between 2-5 and 1.5-5.5 min sputter time, respectively, and then converted to at.% O using the bulk density of TiN (5.21 g/cm³).²⁹

This is the author's peer reviewed, accepted manuscript. However, the online version of record will be different from this version once it has been copyedited and typeset.
PLEASE CITE THIS ARTICLE AS DOI: 10.1116/6.0000454

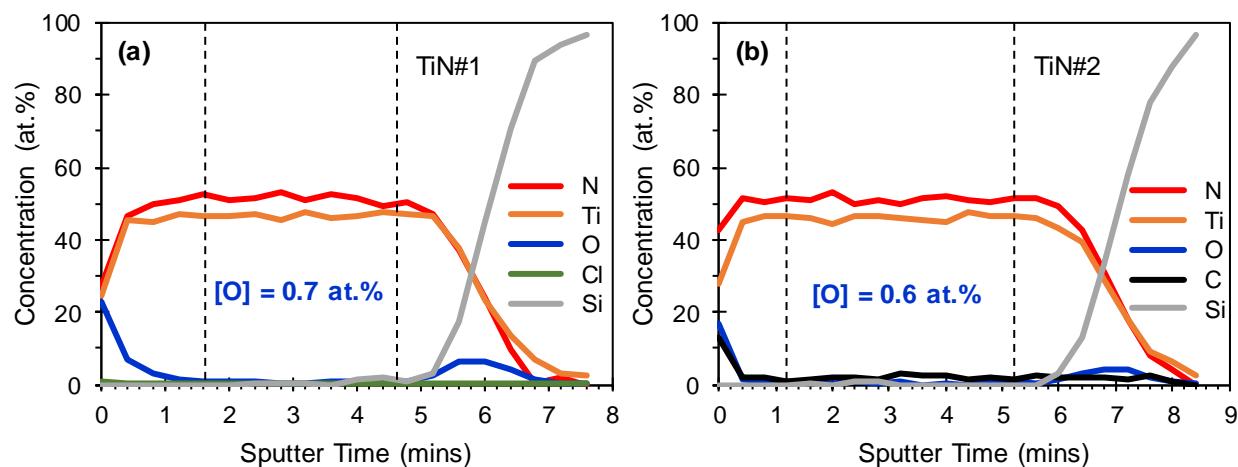


FIG. 6. XPS depth profiles for TiN_x PEALD using (a) TiCl_4 and $\text{Ar-N}_2\text{-H}_2$ plasma at 350°C substrate temperature and (b) TDMAT and Ar-N_2 plasma at 250°C substrate temperature demonstrating < 1 at.% O in the bulk of the films.

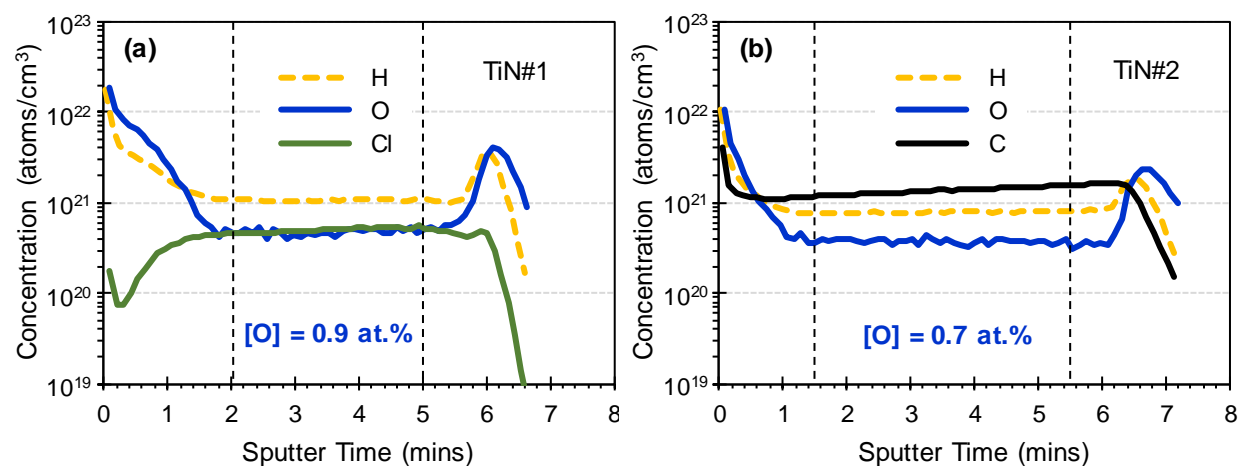


FIG. 7. SIMS depth profiles for TiN_x PEALD using (a) TiCl_4 and $\text{Ar-N}_2\text{-H}_2$ plasma at 350°C substrate temperature and (b) TDMAT and Ar-N_2 plasma at 250°C substrate temperature demonstrating < 1 at.% bulk oxygen content consistent with XPS results.



The bulk average for TiN#1 in Fig. 7(a) is 0.9 at.% O, and for TiN#2 in Fig. 7(b) the bulk average is 0.7 at.% O, in good agreement with the XPS bulk averages. The nitrogen to titanium (N:Ti) ratio for both films was estimated to be 1.1 ± 0.1 (~5% nitrogen rich). Other impurities were also detected. TiN#1 contained 0.2-1 at.% chlorine (Cl) and 2.1 at.% hydrogen (H) in the bulk of the film. TiN#2 contained 1.9-2.7 at.% C and slightly less hydrogen (1.5 at.% H). Silicon was not detected by XPS in the bulk of the films, or quantified by the SIMS measurements. Table II provides a summary of the quantitative XPS and SIMS results for TiN_x PEALD. The reported uncertainties represent the $\pm 1\sigma$ variation associated with at.% averages over the specified range.

TABLE II. Summary of quantitative XPS and SIMS results for TiN_x PEALD.

Material	Technique	Ti (at.%)	N (at.%)	O (at.%)	Cl (at.%)	H (at.%)
TiN#1	XPS	47 ± 1	52 ± 1	0.7 ± 0.2	0.2 ± 0.1	-
TiN#1	SIMS	-	-	0.9 ± 0.08	1.0 ± 0.05	2.1 ± 0.03
TiN#2	XPS	46 ± 1	51 ± 1	0.6 ± 0.4	1.9 ± 0.6	-
TiN#2	SIMS	-	-	0.7 ± 0.05	2.7 ± 0.23	1.5 ± 0.03

The AlN_x and SiN_x XPS depth profiles in Fig. 8 also reveal bulk oxygen content below 1 at.%. In particular, the bulk average oxygen concentration for AlN_x is 0.7 at.% in Fig. 8(a). In this case, the oxygen content was averaged between 2-6 min sputter time. The estimated nitrogen to aluminum (N:Al) ratio was 0.94 ± 0.1 (~3 % Al rich). The SiN_x film contained 0.4 at.% O as indicated in Fig. 8(b). The at.% O for SiN_x was averaged between 1.5-6 min sputter time.

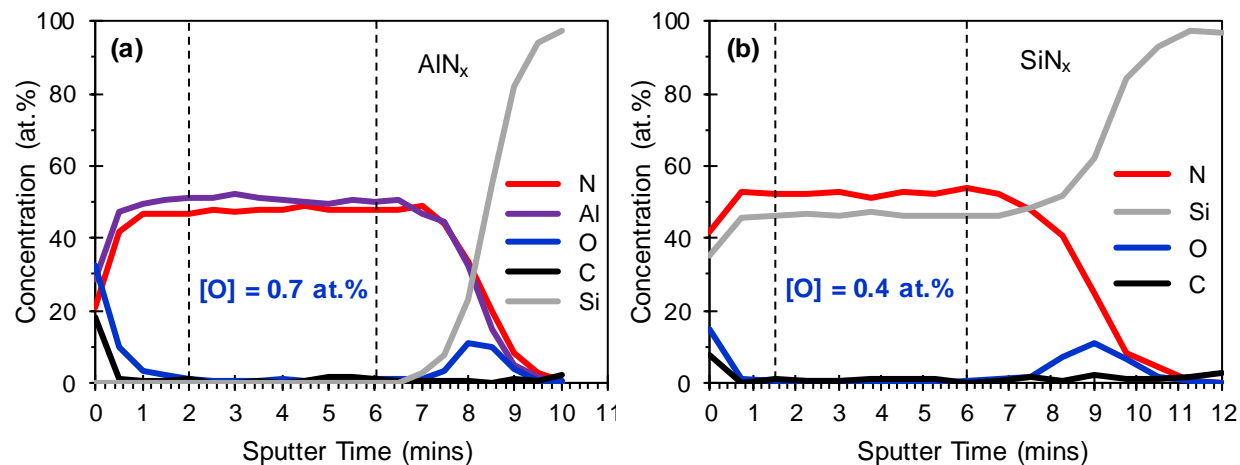


FIG. 8. XPS depth profiling for (a) AlN_x PEALD using TMA and Ar-N₂ plasma at 300°C substrate temperature and (b) SiN_x PEALD using 3DMAS and Ar-N₂ plasma at 350°C substrate temperature where both data sets reveal < 1 at.% O in the bulk of the film.

The estimated N:Si ratio was 1.2 ± 0.1 (~7% nitrogen rich). Both films contained carbon levels below 1 at.%. Silicon was not detected by XPS in the bulk of the AlN_x film. The quantitative XPS results for these films are summarized in Table III. The reported uncertainties represent the $\pm 1\sigma$ variation associated with at.% averages over the specified range.

TABLE III. Summary of quantitative XPS results for AlN_x and SiN_x PEALD.

Material	Al (at.%)	Si (at.%)	N (at.%)	O (at.%)	C (at.%)
AlN _x	51 ± 1	-	48 ± 1	0.7 ± 0.3	0.7 ± 0.7
SiN _x	-	46 ± 1	53 ± 1	0.4 ± 0.1	0.7 ± 0.4

These TiN_x, AlN_x and SiN_x depth profiles demonstrate low oxygen content. However, the films still contained 0.4-0.9 at.% O in the bulk. Another potential source of background oxygen

impurities is plasma etching of the fused silica tube used for RF signal transmission. Etching of SiO₂ by H₂ plasma has been reported in the literature.^{11,30,31} The ICP source used for this work is shown in Fig. 9(a). The reduced transparency of the fused silica tube observed in Fig. 9(a) is indicative of plasma etching. TiN_x growth utilized a mixture of Ar-H₂-N₂ plasma (TiN#1) and Ar-N₂ plasma (TiN#2). Similar to TiN#2, PEALD of AlN_x and SiN_x used Ar-N₂ plasma with no H₂ component. The oxygen content measured by XPS for TiN#1, TiN#2 and AlN_x was similar (i.e., 0.6-0.7 at.%) which is near (or at) the background level. The SiN_x oxygen content was slightly lower (0.4 at.%) and should be considered XPS background. However, similar bulk oxygen content was confirmed by SIMS for TiN#1 (0.9 at.% O with H₂ plasma) and TiN#2 (0.7 at.% O without H₂ plasma). Since all other sources of background oxygen impurities in the reactor were addressed (i.e., system leaks, process gases, elastomer permeation, process pump back-diffusion and outgassing), these results suggest that etching of the fused silica plasma tube might occur with and without the H₂ plasma component. In addition to reactive (or chemical) etching, physical etching can also occur as a result of capacitive coupling within the ICP source.⁶

Physical (or sputter) etching occurs as a result of ion acceleration across the plasma sheath formed on exposed surfaces. As illustrated in Fig. 9(b), a plasma sheath develops to balance the flow of positive (n_i) and negative (n_e) charge to surfaces directly exposed to the plasma. For an inductive plasma, sheath voltages typically range from 20-40 Volts and are a few Debye lengths in width.³² However, increased transient voltages are likely during PEALD at various stages of the plasma dose/exposure steps, resulting in a more capacitive component to the plasma with a higher sputter yield (e.g., during initial lighting of the plasma). The plasma appeared well contained within ICP tube during plasma dose steps, and no optical emission was observed above the substrate surface. Since transient voltages are expected to be relatively short, however, the

plasma generated by an increase in capacitive coupling may not be easily observed. As discussed in the previous section, ion bombardment during growth has been shown to reduce oxygen content in nitride films.^{25,26} To minimize background impurities due to reactive and/or physical etching of the plasma tube, an alternative tube material is needed. Sapphire is well known for its chemical stability and low sputter yield. Reduced levels of oxygen in silicon and TiN_x films using a sapphire plasma tube (vs. quartz/fused silica) with H_2 plasma have been demonstrated.^{33,34} Further reduction in background oxygen impurities is expected by replacing the fused silica plasma tube with sapphire.

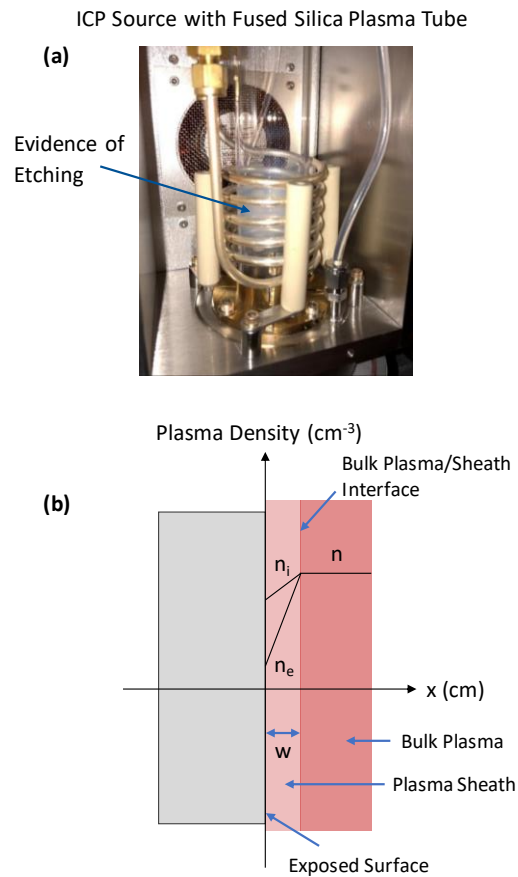


FIG. 9. (a) The fused silica ICP tube used for this work shows evidence of plasma etching as indicated by the reduced transparency within the region of the RF coil. (b) A plasma sheath is formed on surfaces exposed directly to plasma resulting in ion acceleration toward the surface.

IV. CONCLUSIONS

In summary, this work identified the various sources of background oxygen impurities and systematically described the measures taken to achieve UHP reactor conditions (i.e., partial pressures $< 10^{-8}$ Torr for background oxygen species). In situ ellipsometry measurements during and after TiN_x PEALD revealed the effects of oxygen incorporation on film resistivity due to impurities in the process gas, emphasizing the importance of process gas purification for creating and maintaining UHP conditions. In addition, modeling was used to show that permeation through elastomer seals must be eliminated. TiN_x , AlN_x and SiN_x films by PEALD with low oxygen content (< 1 at.%) demonstrated the effectiveness of UHP conditions for high purity nitride film growth. The fused silica plasma tube used for this work showed evidence of plasma etching. Further improvements in nitride film quality are anticipated by replacing the fused silica plasma tube with sapphire.

¹C. Fenouillet-Beranger et al., Solid State Electron. **53**, 730 (2009).

²V. Djara, V. Deshpande, M. Sousa, D. Caimi and L. Czornomaz, IEEE Electr. Device Lett. **37**, 169 (2016).

³Y. Lu, Q. Jiang, Z. Tang, S. Yang, C. Liu and K. J. Chen, Appl. Phys. Express **8**, 064101 (2015).

⁴K. J. Voon, K. M. Bothe, P. Motamedi, K. C. Cadien and D. W. Barlage, J. Phys. D Appl. Phys. **47**, 345104 (2014).

⁵K. Kim, M. Hua, D. Liu, J. Kim, K. J. Chen and Z. Ma, Nano Energy **43**, 259 (2018).

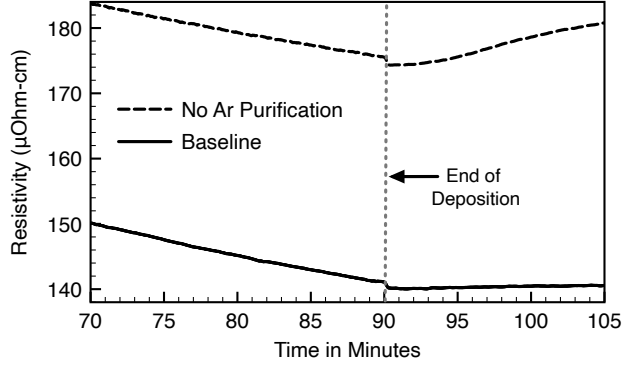
⁶H. C. M. Knoops, T. Faraz, K. Arts and W. M. M. Kessels, J. Vac. Sci. Technol. A **37**, 030902 (2019).

- ⁷P. Caubet et al., J. Electrochem. Soc. **155**, H625 (2008).
- ⁸J. Musschoot, Q. Xie, D. Deduytsche, S. Van den Berghe, R. L. Van Meirhaeghe and C. Detavernier, Microelectron. Eng. **86**, 72 (2009).
- ⁹C. J. Brennan, C. M. Neumann and S. A. Vitale, J. Appl. Phys. **118**, 045307 (2015).
- ¹⁰M. J. Sowa, L. Ju, A. C. Kozen, N. C. Strandwitz, G. Zeng, T. F. Babuska, Z. Hsain and B. A. Krick, J. Vac. Sci. Technol. A **36**, 06A103 (2018).
- ¹¹I. Krylov, X. Xu, E. Zoubenko, K. Weinfeld, S. Boyeras, F. Palumbo, M. Eizenberg and D. Ritter, J. Vac. Sci. Technol. A **36**, 06A105 (2018).
- ¹²H. H. Sønsteby, A. Yanguas-Gil and J. W. Elam, J. Vac. Sci. Technol. A **38**, 020804 (2020).
- ¹³P. Patsalas, N. Kalfagiannis and S. Kassavetis, Materials **2015**, 3128 (2015).
- ¹⁴E. Langereis, S. B. S. Heil, M. C. M. van de Sanden and W. M. M. Kessels, J. Appl. Phys. **100**, 023534 (2006).
- ¹⁵S. Logothetidis and A. Barborica, Microelectron. Eng. **33**, 309 (1997).
- ¹⁶J. F. O'Hanlon, *A User's Guide to Vacuum Technology*, 3rd ed. (Wiley, NJ, 2003).
- ¹⁷A. Roth, *Vacuum Technology*, 3rd ed. (North-Holland, Netherlands, 1990).
- ¹⁸B. Craster and T. G. J. Jones, Polymers **2019**, 1056 (2019).
- ¹⁹T. C. Chivers and A. F. George, 14th International Symposium on the Packaging and Transportation of Radioactive Materials (PATRAM 2004), Berlin, Germany, Sept. 20-24 (2004).
- ²⁰C. Ma, E. Shero, N. Verma, S. L. Gilbert and F. Shadman, J. IES **38**, 43 (1995).
- ²¹M. Sefa and J. Setina, J. Vac. Sci. Technol. A **35**, 041603 (2017).
- ²²B. S. Meyerson, Appl. Phys. Lett. **48**, 797 (1986).
- ²³B. S. Meyerson, U.S. Patent No. 5,298,452 (29 March 1994).

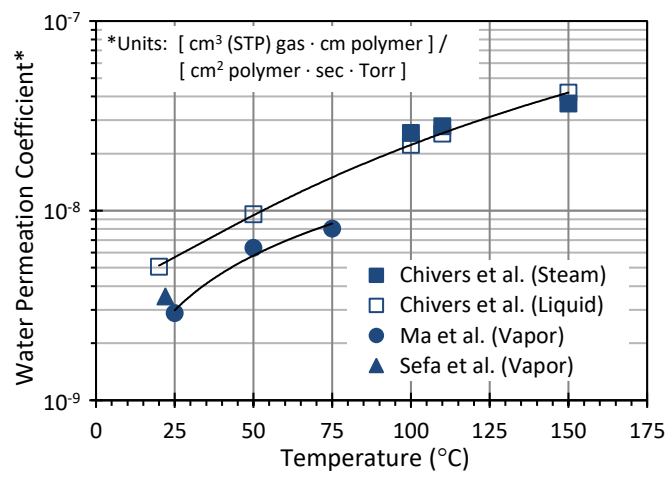
- ²⁴H. B. Profijt and W. M. M. Kessels, ECS Transactions **50**, 23 (2012).
- ²⁵S. Karwal, M. A. Verheijen, B. L. Williams, T. Faraz, W. M. M. Kessels and M. Creatore, J. Mater. Chem. C **6**, 3917 (2018).
- ²⁶T. Faraz et al., ACS Appl. Mater. Inter. **10**, 13158 (2018).
- ²⁷J. W. Elam, M. D. Groner and S. M. George, Rev. Sci. Instrum. **73**, 2981 (2002).
- ²⁸G. B. Rayner Jr, U.S. Patent No. 9,695,510 B2 (4 July 2017).
- ²⁹J. R. Rumble, ed., *CRC Handbook of Chemistry and Physics*, 101st Edition, Internet Version (CRC Press/Taylor & Francis, Boca Raton, 2020).
- ³⁰R. P. H. Chang, C. C. Chang and S. Darack, J. Vac. Sci. Technol. **20**, 45 (1982).
- ³¹O. Peña, S. Muhl, W. López, L. Rodríguez-Fernández and J. L. Ruvalcaba-Sil, Thin Solid Films **518**, 3156 (2010).
- ³²M. A. Lieberman and A. J. Lichtenberg, *Principles of Plasma Discharges and Materials Processing*, 2nd ed. (Wiley, NJ, 2005).
- ³³N. M. Johnson, J. Walker, C. M. Doland, K. Winer and R. A. Street, Appl. Phys. Lett. **54**, 1872 (1989).
- ³⁴I. Krylov, X. Xu, K. Weinfeld, V. Korchnoy, D. Ritter and M. Eizenberg, J. Vac. Sci. Technol. A **37**, 010906 (2019).



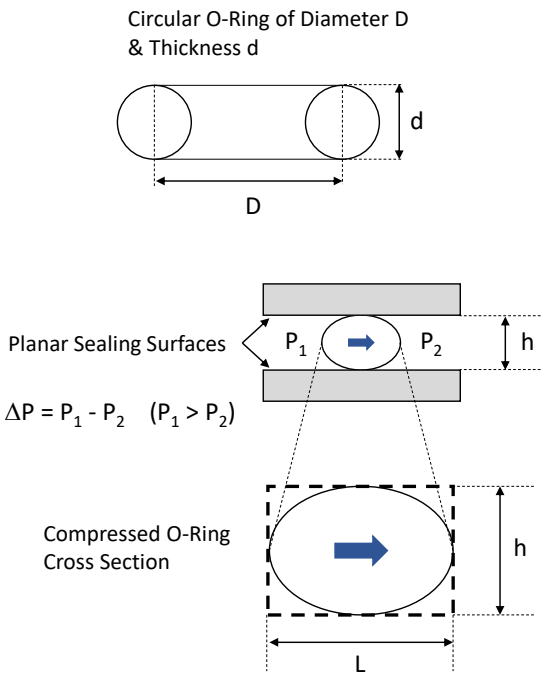
This is the author's peer reviewed, accepted manuscript. However, the online version of record will be different from this version once it has been copyedited and typeset.
PLEASE CITE THIS ARTICLE AS DOI: 10.1116/6.0000454



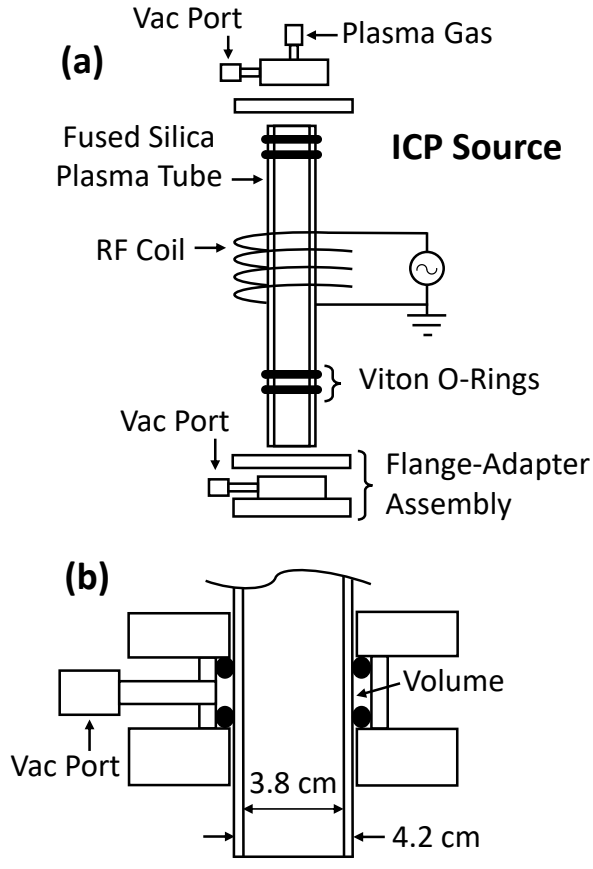
This is the author's peer reviewed, accepted manuscript. However, the online version of record will be different from this version once it has been copyedited and typeset.
PLEASE CITE THIS ARTICLE AS DOI: 10.1116/1.50000454



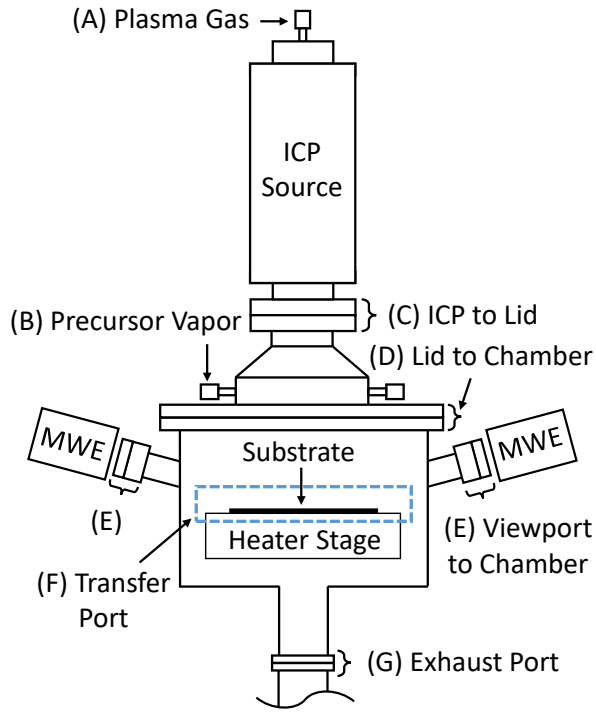
This is the author's peer reviewed, accepted manuscript. However, the online version of record will be different from this version once it has been copyedited and typeset.
PLEASE CITE THIS ARTICLE AS DOI: 10.1116/6.0000454



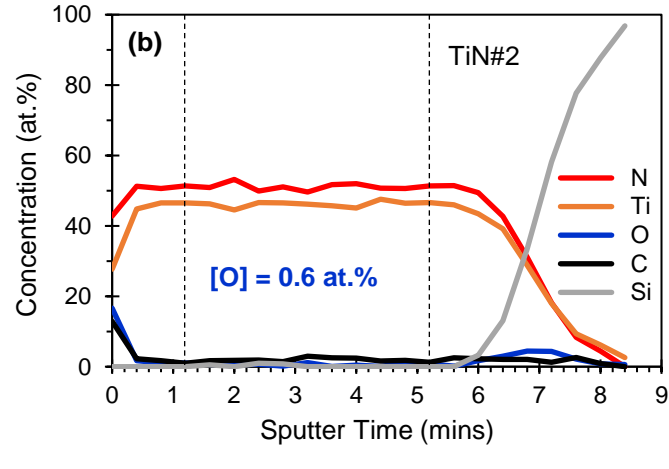
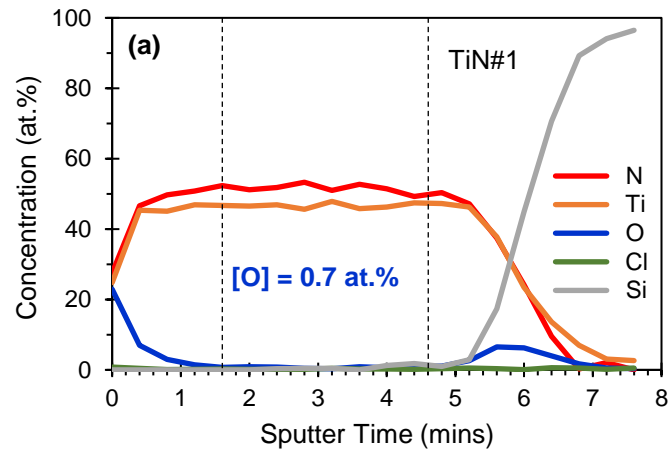
This is the author's peer reviewed, accepted manuscript. However, the online version of record will be different from this version once it has been copyedited and typeset.
PLEASE CITE THIS ARTICLE AS DOI: 10.1116/6.0000454



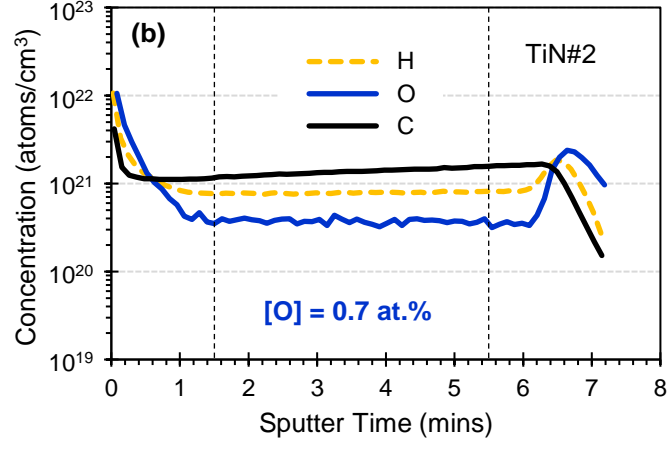
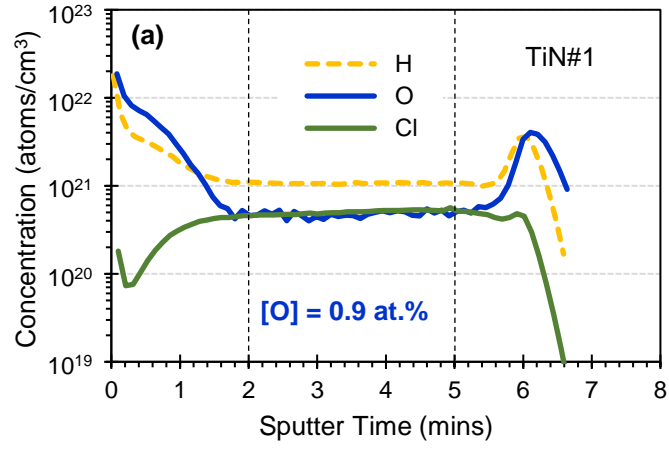
This is the author's peer reviewed, accepted manuscript. However, the online version of record will be different from this version once it has been copyedited and typeset.
PLEASE CITE THIS ARTICLE AS DOI: 10.1116/6.0000454



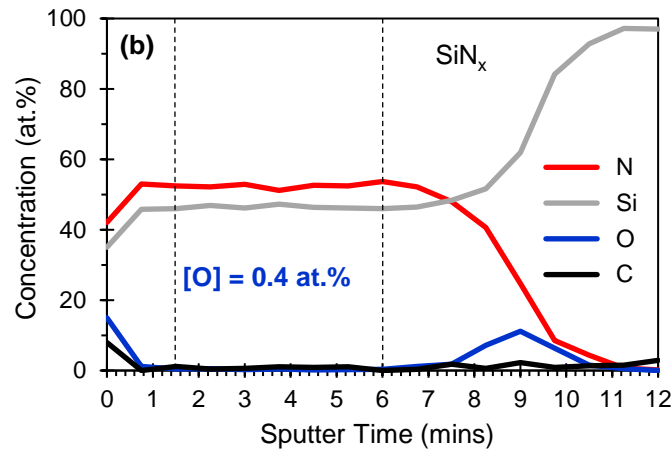
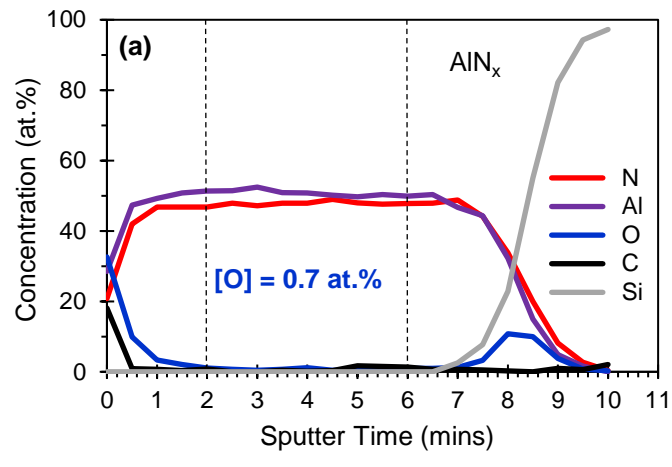
This is the author's peer reviewed, accepted manuscript. However, the online version of record will be different from this version once it has been copyedited and typeset.
PLEASE CITE THIS ARTICLE AS DOI: 10.1116/1.6.0000454



This is the author's peer reviewed, accepted manuscript. However, the online version of record will be different from this version once it has been copyedited and typeset.
PLEASE CITE THIS ARTICLE AS DOI: 10.1116/6.0000454



This is the author's peer reviewed, accepted manuscript. However, the online version of record will be different from this version once it has been copyedited and typeset.
PLEASE CITE THIS ARTICLE AS DOI: 10.1116/1.5000454



This is the author's peer reviewed, accepted manuscript. However, the online version of record will be different from this version once it has been copyedited and typeset.
PLEASE CITE THIS ARTICLE AS DOI: 10.1116/6.0000454

ICP Source with Fused Silica Plasma Tube

